ACS OMEGA

http://pubs.acs.org/journal/acsodf

Article

Computational Study of CO_2 Reduction Catalyzed by Iron(I) Complex at Different Spin States: Cooperativity of Hydrogen Bonding and Auxiliary Group Effect

Yazhou Li, Xuhui Lin, Fang Ma,* and Yirong Mo*

Cite This: *ACS Omega* 2021, 6, 31971−31981

Read Online

ACCESS | Metrics & More | Article Recommendations | Supporting Information

ABSTRACT: To explore alternative approaches to the CO_2 reduction to formate and provide an insight into the spin state effect on the CO_2 reduction, we theoretically designed a kind of low-valence iron(I) model complex, whose doublet, quartet, and sextet states are denoted as ^{2}**Fe(I)**, ^{4}**Fe(I)**, and ^{6}**Fe(I)**, respectively. This complex is featured with an iron(I) center, which bonds to a 1,2-ethanediamine (en) and a 2-hydroxy-biphenyl group. Reaction mechanisms for the CO_2 reduction to formate catalyzed by this iron(I) model complex were explored using density functional theory (DFT) computations. Studies showed that the univalent iron(I) compound can efficiently fix and activate a CO_2 molecule, whereas its oxidized forms with trivalent iron(III) or bivalent iron(II) cannot activate CO_2. For the iron(I) compound, it was found that the lowest spin state ^{2}**Fe(I)** is the most favorable for the CO_2 reduction as the reactions barriers involving ^{2}**Fe(I)**, ^{4}**Fe(I)**, and ^{6}**Fe(I)** are 25.6, 37.2, and 35.9 kcal/mol, respectively. Yet, a photosensitizer-free visible-light-mediated high−low spin shift from ^{4}**Fe(I)** and ^{6}**Fe(I)** to ^{2}**Fe(I)** is likely through the reverse intersystem crossing (RIC) because the ^{4}**Fe(I)** and ^{6}**Fe(I)** compounds have strong absorption in the visible-light range. Notably, the synergistic interaction between the hydrogen bonding from the auxiliary hydroxyl group in the 2-hydroxy-biphenyl moiety to CO_2 and an intermediate five-membered ring promotes the proton transfer, leading to the formation of the −COOH moiety from CO_2 and the Fe−O bond. With the addition of H_2, one H_2 molecule is split by the Fe−O bond and thus serves as H atom sources for both the CO_2 reduction and the recovery of the auxiliary hydroxyl group. The present theoretical study provides a novel solution for the challenging CO_2 reduction, which calls for further experimental verifications.

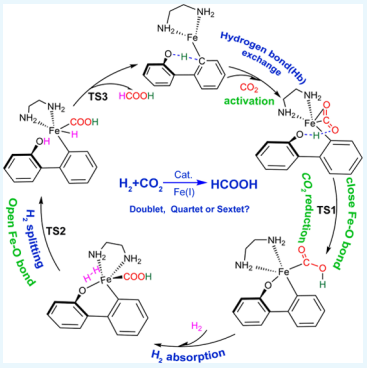

INTRODUCTION

Excessive CO_2 has been released into the atmosphere due to the large-scale fossil fuel consumption. This has generated detrimental environmental consequences and forced us to mitigate the impacts of CO_2 and prepare for potential energy crises. The ideal solution is the cyclic utilization of CO_2, which serves as a cheap, abundant, and nontoxic C1 building block for value-added chemicals. To this end, the CO_2 hydrogenation with 100% atom economy to formic acid and its derivatives is a particularly significant and promising route.[1−3] In the past two decades, steady progresses have been achieved in exploring diverse routes of homogeneous catalytic hydrogenation of CO_2. However, the majority of reported catalysts are based on noble metals, such as rhodium,[4,5] ruthenium,[6−8] and iridium,[9,10] which do not meet economic sustainability and environmental safety, and further, their uses require very demanding conditions such as high temperature and/or acidic solutions. Consequently, there are growing interests in developing catalytic systems using earth-abundant and non-noble (base) metals. For instances, base-metal catalysts based on iron,[11,12] cobalt,[13,14] nickel,[15] copper,[16,17] and manganese[18] have been employed to catalyze the hydrogenation of CO_2, but their catalytic performances so far are well below those based on precious transition metals. Therefore, it is highly desirable to develop high-efficient and low-cost base-metal catalysts to produce useful chemical feedstock such as formic acid from CO_2 and H_2.

Indeed, the exploration of high-efficient iron-based catalysts is a very active research field since iron is one of the most abundant and cheapest base metals on Earth. The uniqueness of iron lies in its variable oxidation states (I, II, and III) and high- and low-spin states in its complexes. Recent studies showed that the regulation of the oxidation state of catalysts is an important strategy for designing better-performing catalysts for the CO_2 reduction.[19] Complexes with the iron oxidation state II or III have been extensively tested. For instances, the groups of Laurenczy and Beller,[20,21] Milstein,[22] Gonsalvi,[23,24] Hazari and Bernskoetter,[25,26] etc. have developed several well-

Received: August 30, 2021
Accepted: November 2, 2021
Published: November 16, 2021

https://doi.org/10.1021/acsomega.1c04758
ACS Omega 2021, 6, 31971−31981

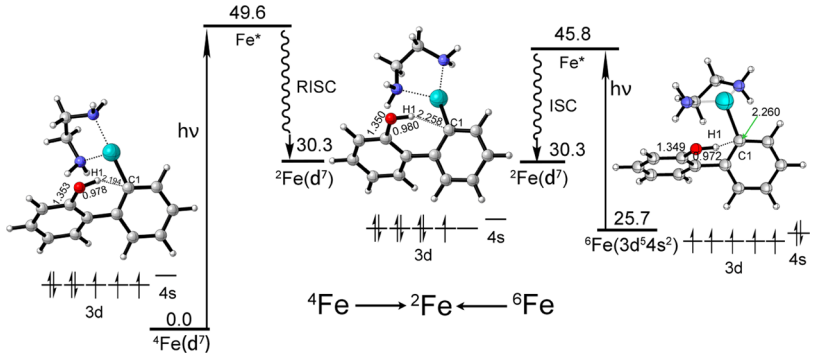

Figure 1. Optimized structures of the designed iron(I)-based complex at the spin states ^{2}**Fe**, ^{4}**Fe**, and ^{6}**Fe**. The bond lengths are in Å, and the free energies are in kcal/mol.

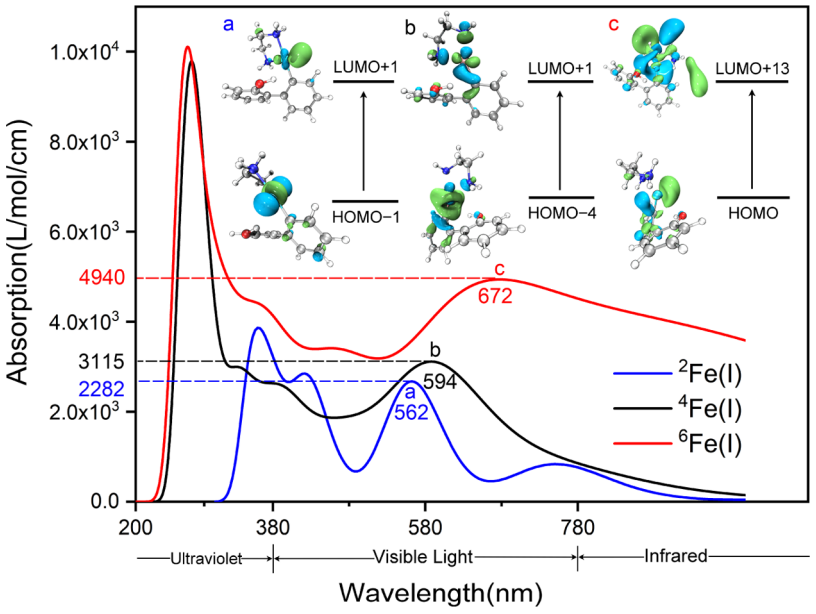

Figure 2. Simulated UV−vis absorption spectroscopies and the designated d−d transitions in the range of visible light.

defined phosphine iron complexes, which can catalyze the hydrogenation of CO_2 to formic acid. The Zhu[27] and Renaud[28] groups independently reported the hydrogenation of CO_2 to formate catalyzed by phosphine-free iron cyclopentadienone (IC) complex under an air- and moisture-tolerant environment. Yang et al. further revealed a self-promoted mechanism of this reaction by performing density functional theory (DFT) computations.[29]

Compared to the oxidation states II and III, iron (I) complexes are relatively few and have been less investigated, though in the literature they have been employed to catalyze certain reactions without the participation of CO_2. For example, there are C−H bond aminations catalyzed by $(Ar^L)Fe^I$ (Ar^L = 5-mesityl-1,9-(2,4,6-$Ph_3C_6H_2$)dipyrrin)[30] and N_2 fixation and activation using nitrogenase or its mimics.[31] However, to the best of our knowledge, the CO_2 reduction catalyzed by iron(I) compounds is seldom reported and only applied to certain limited systems, for example, electrochemical conversion of CO_2 to CO catalyzed by iron complexes with an N_2O_2-type *N*,*N*′-bis(salicylaldehyde)-1,2-phenylenediamine salophen ligand.[32] Thus, it is interesting and valuable to gain a deep insight into the CO_2 reduction catalyzed by iron(I) compounds and to expand the applications of inexpensive iron-based catalysts. Regarding the less common iron(I) complexes, additional ligands are often required to stabilize the metal center. In recent years, multiform ligands have been experimentally synthesized and employed to stabilize the central Fe^+ ion in several $3d^7$/$3d^5$4s^2 high-spin iron(I) complexes, for example, 3,6-di-*tert*-butyl-1,8-bis((ditert-butylphosphino)methyl)-carbazole,[33] 5-mesityl-1,9-(2,4,6-$Ph_3C_6H_2$)dipyrrin,[30] 1,3-dicyclohexylimidazol-2-ylidene (ICy),[34] and *N*-heterocyclic carbenes (NHCs).[35]

To explore the potential applications of iron(I)-based catalytic systems to the CO_2 reduction, here, we theoretically designed a kind of low-valence iron(I) model complex where the iron(I) center binds to an ethanediamine (en) and a 2-hydroxy-biphenyl group. This model system can exist in three spin states, doublet ^{2}**Fe(I)**, quartet ^{4}**Fe(I)**, and sextet ^{6}**Fe(I)**. The selection of 2-hydroxy-biphenyl is based on the reported gold(I) complex with a phosphine-free protonated 2-(2-pyridyl)-phenyl ligand,[36] except that we replaced the protonated 2-(2-pyridyl) group with a phenol, which contains a hydroxyl group. The role of ethanediamine is to safeguard the "naked" iron(I) species by improving the stabilities of ^{2}**Fe(I)**, ^{4}**Fe(I)**, and ^{6}**Fe(I)**. In this work, the hydrogenation of CO_2 to formate catalyzed by the above-designed low-valence iron(I) catalyst was investigated by performing DFT

https://doi.org/10.1021/acsomega.1c04758
ACS Omega 2021, 6, 31971−31981

calculations, aiming at providing a novel idea of iron-based catalyst design for the CO_2 reduction.

RESULTS AND DISCUSSION

Geometries of ^{2}Fe(I), ^{4}Fe(I), and ^{6}Fe(I) States with Intramolecular Hydrogen Bonding and Spin Shift among Spin States. Iron-based complexes with distinctive electronic and coordinative unsaturation usually possess enhanced reactivity in certain reactions and play an important role as either reagents or catalysts.[37,38] Our interest here is in iron complexes with the less common iron(I) oxidation state ($3d^7$ and $3d^54s^2$), as we intend to gain an insight into their electronic structure characteristics and explore their potential applications in the CO_2 reduction. To achieve these goals, we designed a low-valence iron(I) model complex, where the iron(I) center binds to an ethanediamine (en) and a 2-hydroxy-biphenyl group. Figure 1 depicts the optimized structures of this iron(I)-based complex at the doublet state **^{2}Fe(I)**, the quartet state **^{4}Fe(I)**, and the sextet state **^{6}Fe**. Interestingly, it is found that the ground state of the low-valence iron(I) model complex is the quartet state **^{4}Fe**. Although the doublet state **^{2}Fe** and the sextet state **^{6}Fe** have higher energies by 30.3 and 25.7 kcal/mol than **^{4}Fe**, their geometric parameters are very close (see Figure 1). The plots of the spin density at the three states revealed the similar localizations of the most spin density (unpaired electrons) around the metal center (see Figure S1 in the Supporting Information).

We looked into the electronic excitation properties of the iron(I)-based complex involving **^{2}Fe(I)**, **^{4}Fe(I)**, and **^{6}Fe(I)**, in virtue of simulated UV−vis absorption spectroscopy. As depicted in Figure 2, the maximum absorption is in the range of ultraviolet for all three states. The maximum absorption intensities for **^{4}Fe(I)** and **^{6}Fe(I)** are almost 3 times higher than that for **^{2}Fe(I)**. Of particular, in the range of visible light, there is a secondary maximum absorption near 580 nm wavelength for **^{2}Fe(I)** and **^{4}Fe(I)**, respectively, and the corresponding absorption intensity for **^{4}Fe(I)** is about 1.5 times higher than that for **^{2}Fe(I)**. There is a secondary maximum absorption near 670 nm wavelength for **^{6}Fe(I)**, and its absorption intensity is 2 times higher than that for **^{2}Fe(I)**. Since **^{4}Fe(I)** and **^{6}Fe(I)** have much stronger excitations through d−d transition than **^{2}Fe(I)**, there is a possibility for the photosensitizer-free visible-light-mediated high−low spin shift from the stable quartet or sextet state to the less stable doublet state through reverse intersystem crossing (RISC)[39,40] (see Figure 1). Here, it should be mentioned that RISC is usually defined as a process of energy transfer from the excited triplet (high) state back to the singlet (low) state in previous studies.[40] In addition, vertical ionization energies (IE) are calculated at the M06/6-311+G(d,p)/def2tzvp level to be 6.43, 6.67, and 4.67 eV for **^{2}Fe(I)**, **^{4}Fe(I)**, and **^{6}Fe(I)**, respectively.

It should be noted that the distance between the hydrogen of the hydroxyl group and the carbon bonding to Fe(I) (H1−C1) is about ∼2.2 Å at all **^{2}Fe(I)**, **^{4}Fe(I)**, and **^{6}Fe(I)** states (marked in Figure 1), which is much shorter than the sum of van der Waals radius between C and H atoms (∼2.9 Å). Thus, it is safe to say that there is an intramolecular hydrogen bond O−H···C, where the O−H bond (∼0.98 Å) is slightly stretched, compared with the value in phenol (0.960 Å) and in 2-hydroxy-biphenyl (0.964 Å). Like normal hydrogen bonds, the stretching vibrations of the O−H bond are red-shifted by 447, 333, and 117 cm^{-1} for the **^{2}Fe(I)**, **^{4}Fe(I)**, and **^{6}Fe(I)** states, respectively, with the reference of 2-hydroxy-biphenyl (3816 cm^{-1}). To further validate the formation of the hydrogen bond O−H···C, electrostatic potentials (ESPs) near the hydroxyl group and the C atom were examined, as shown in Figure 3. ESP can be used to analyze the sites of

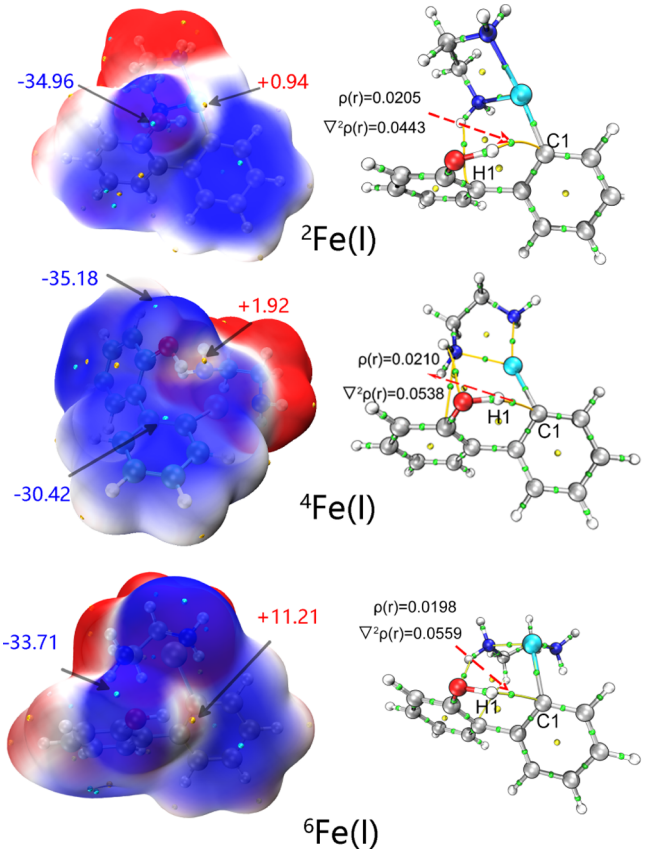

Figure 3. ESP maps (left) and BCP figures (right) of the spin states **^{2}Fe(I)**, **^{4}Fe(I)**, and **^{6}Fe(I)**. In both ESP maps and BCP figures, sky blue dots represent the local minima of ESP and yellow dots denote the maxima of ESP.

electrophilic and nucleophilic attacks based on its negative and positive ESP values, respectively. Sites with minimum ESP were generally prone to electrophilic attack. As depicted in Figure 3, on the one hand, the local minimum ESP values can be observed near the marked C atom region (V_{min} = −31.1 kcal/mol in **^{2}Fe(I)**, −30.4 kcal/mol in **^{4}Fe(I)**, and −33.7 kcal/mol in **^{6}Fe(I)**), which can act as a hydrogen-bond receptor. On the other hand, the local maximum ESP values can be observed near the H atom region of the marked hydroxyl group (V_{max} = 0.9 kcal/mol in **^{2}Fe(I)**, 1.9 kcal/mol in **^{4}Fe(I)**, and 11.2 kcal/mol in **^{6}Fe(I)**), which can act as a weak hydrogen-bond donor. From the electrostatics point of view, we inferred that the hydrogen bond O−H···C was formed between the marked C atom and the H atom of the marked hydroxyl. The formed hydrogen bond was also examined with the quantum chemical topology method (QTAIM). The bond critical points (BCPs) and bond paths were obtained with the program Multiwfn[41,42] and are illustrated in Figure 3. Obviously, there are BCPs between the two interacting atoms of the marked C and H atoms, which are connected by the corresponding bond paths. Figure 3 also lists the electron density (ρ) and Laplacian ($\nabla^2\rho$) values at BCPs, which fall into the range of the criteria for the

https://doi.org/10.1021/acsomega.1c04758
ACS Omega 2021, 6, 31971−31981

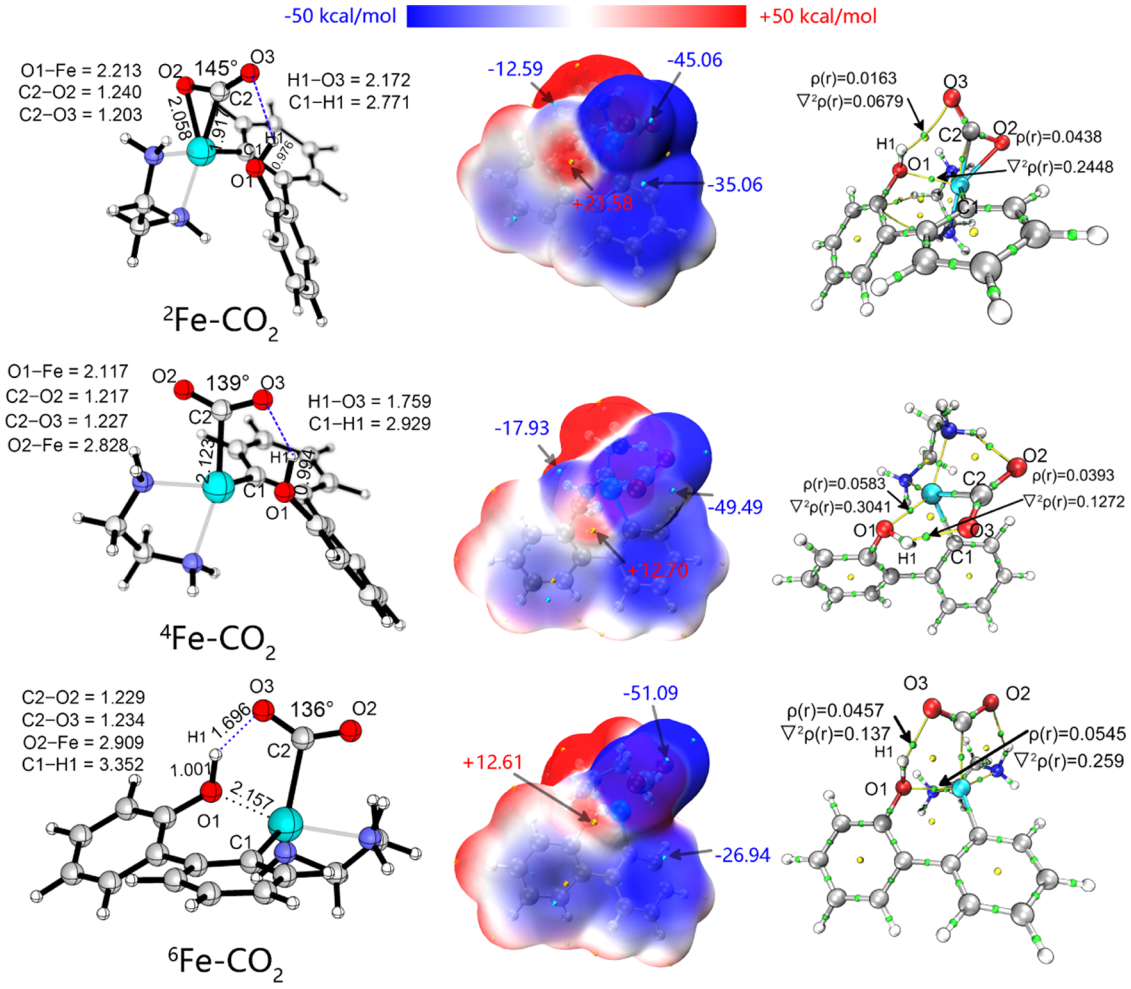

Figure 4. Optimized structures (left), ESP maps (middle), and BCP figures (right) of ^{2}**Fe-CO$_2$**, ^{4}**Fe-CO$_2$**, and ^{6}**Fe-CO$_2$**. The bond lengths are in Å. In ESP maps and BCP figures, sky blue dots represent the local minima of EPS and yellow dots denote the maxima of EPS.

formation of hydrogen bonds proposed by Lipkowski et al. (0.002−0.04 and 0.02−0.15 au for ρ and Laplacian $\nabla^2\rho$).[43] These results confirm the existence of hydrogen bonds O−H···C at all ^{2}**Fe(I)**, ^{4}**Fe(I)**, and ^{6}**Fe(I)** states. Besides, color-mapped RDG isosurface graphs and scatter diagrams of RDG versus sign $(\lambda^2)\rho$ for ^{2}**Fe(I)**, ^{4}**Fe(I)**, and ^{6}**Fe(I)** were also provided in the Supporting Information (see Figure S2 in the Supporting Information). All information concludes that there is a weak hydrogen bond in ^{2}**Fe(I)** and a moderate hydrogen bond in ^{4}**Fe(I)** and ^{6}**Fe(I)**.

Fixation and Activation of CO$_2$ and Hydrogen-Bond Exchange. By adding a CO_2 to the designed iron(I) compound, we performed geometry optimizations to study the fixation and activation of CO_2 at all ^{2}**Fe(I)**, ^{4}**Fe(I)**, and ^{6}**Fe(I)** states. The optimized structures are shown in Figure 4. Significant differences can be observed in the resulting ^{2}**Fe-CO$_2$**, ^{4}**Fe-CO$_2$**, and ^{6}**Fe-CO$_2$** complexes. In ^{2}**Fe-CO$_2$** with the lowest spin state, it is found that the fixation of CO_2 on the Fe center occurs through the d−π coordination. Remarkably, the OCO angle bends to 145°, while the C2═O2 bond involved in the interaction with the Fe center is stretched from 1.155 to 1.240 Å and the C2═O3 bond length is 1.203 Å. But in ^{4}**Fe-CO$_2$** and ^{6}**Fe-CO$_2$** with high spin states, the C2 of CO_2 interacts with the Fe center through single coordination. In ^{4}**Fe-CO$_2$**, the C2═O2 and C2═O3 bond lengths are 1.217 and 1.227 Å, respectively, and the OCO angle bends to 139°. Similarly, in ^{6}**Fe-CO$_2$**, the C2═O2 and C2═O3 bond lengths are 1.229 and 1.234 Å, respectively, and the OCO angle is 136°. These data suggest that the process of the CO_2 fixation on the Fe center is also the process of the CO_2 activation. For comparison, we studied the CO_2 fixation on the same designed Fe complex but with a trivalent iron(III) or a bivalent iron(II) and found that the CO_2 fixation on the Fe center with either II or III oxidation state is only an adsorption process through van der Waals interactions, and CO_2 is thus not activated (see Figure S3 in the Supporting Information).

Interestingly, the CO_2 fixation on the iron(I) complex is an exergonic process with decreasing Gibbs free energies of 11.2 and 11.9 kcal/mol, for excited states ^{2}**Fe** and ^{6}**Fe$_2$**, respectively, but is an endergonic process with increasing Gibbs free energy of 5.9 kcal/mol for the ground state ^{4}**Fe**. The fixation of CO_2 by the iron(I) complex also influences the intramolecular O−H···C hydrogen bonding. Compared with the initial iron(I) complex, C1···H1 distance is greatly increased to 2.771 Å in ^{2}**Fe-CO$_2$**, 2.929 Å in ^{4}**Fe-CO$_2$**, and 3.352 Å in ^{6}**Fe-CO$_2$**, as seen in Figure 4. These long distances suggest the disappearance of the original O−H···C hydrogen bonds with the addition of CO_2. Meanwhile, the distances between O3 and H1 is greatly reduced to 2.172 Å in ^{2}**Fe-CO$_2$**, 1.759 Å in ^{4}**Fe-CO$_2$**, and 1.696 Å in ^{4}**Fe-CO$_2$**, suggesting the formation of a new hydrogen bond O−H···O in all complexes. Therefore, along with the CO_2 fixation on the Fe center, there is an

https://doi.org/10.1021/acsomega.1c04758
ACS Omega 2021, 6, 31971−31981

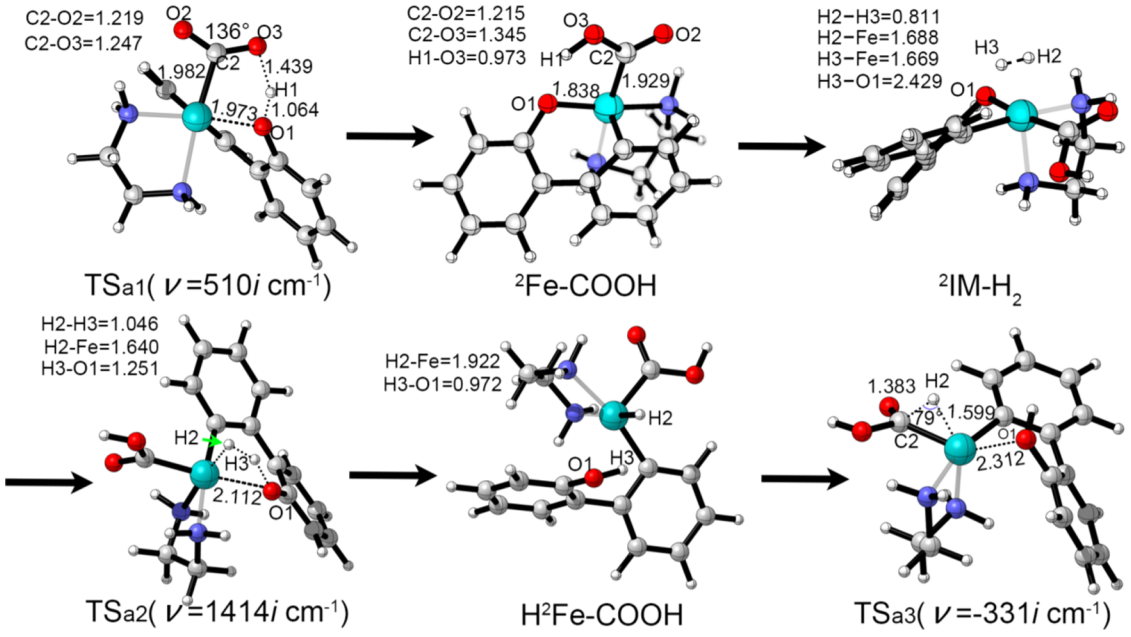

Figure 5. Evolution of optimized structures in the process of CO_2 reduction catalyzed by iron(I)-based complex at the doublet state **^{2}Fe(I)**. The bond distances are given in Å.

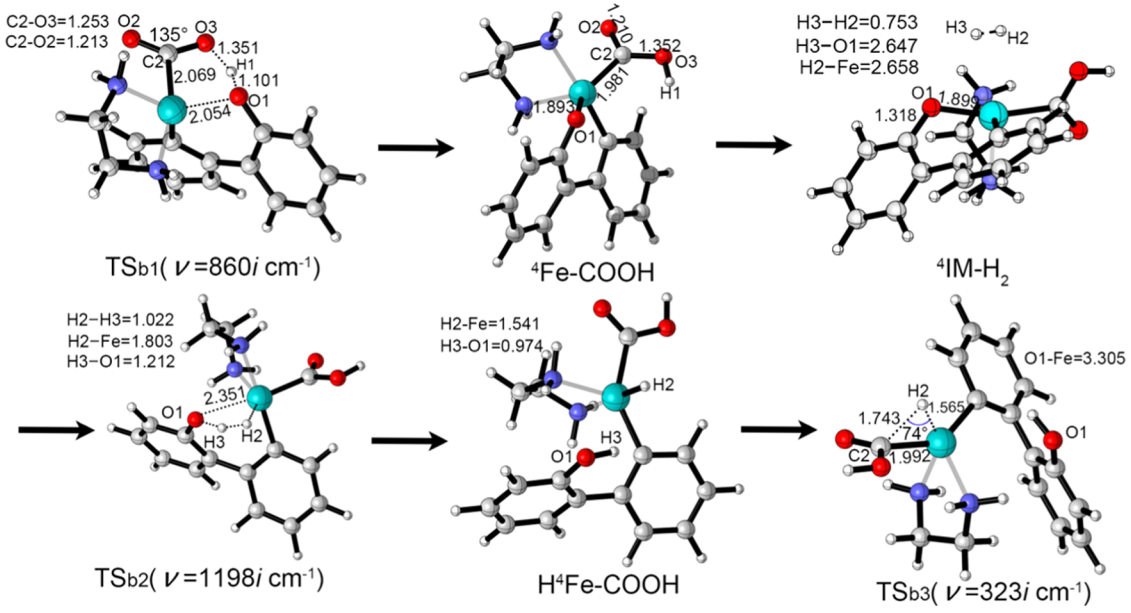

Figure 6. Evolution of optimized structures in the process of CO_2 reduction catalyzed by iron(I)-based complex at the quartet state **^{4}Fe(I)**. The bond distances are given in Å.

interesting shifting of hydrogen bonds from the O−H···C hydrogen bond to the O−H···O hydrogen bond.

In the newly formed hydrogen bond O−H···O3, the stretching vibration of the O−H bond is red-shifted by about 165, 508, and 729 cm^{-1} in the complexes of **^{2}Fe-CO$_2$**, **^{4}Fe-CO$_2$**, and **^{6}Fe-CO$_2$**, respectively, in comparison with the value 3816 cm^{-1} in 2-hydroxy-biphenyl. We also validated the formation of the hydrogen bonds from the electrostatics point of view. The ESPs of **^{2}Fe-CO$_2$**, **^{4}Fe-CO$_2$**, and **^{6}Fe-CO$_2$** are exhibited in Figure 4 (middle). The local minimum ESP values can be observed near the marked O3 atom region (V_{min} = −45.1, −49.5, and −51.1 kcal/mol in **^{2}Fe-CO$_2$**, **^{4}Fe-CO$_2$**, and **^{6}Fe-CO$_2$**), which can act as a hydrogen bond receptor. The local maximum ESP values can be found near the H atom region of the marked hydroxyl group (V_{max} = 21.6, 12.7, and 12.6, respectively), which can act as a hydrogen-bond donor. The electrostatic attraction thus drives the formation of the hydrogen bond O−H···C between the marked O3 atom and the H atom of the marked hydroxyl group. Further, the bond critical points (BCPs) and bond paths depicted in Figure 4 (right) also verified the formed hydrogen bonds. As shown in Figure 4, the BCPs between the two interacting atoms of the marked O3 and H atoms can be identified and connected by the corresponding bond paths. Figure 4 also lists the electron density (ρ) and Laplacian ($\nabla^2\rho$) values for **^{2}Fe-CO$_2$**, which fall in the range of the criteria for the formation of hydrogen bonds (0.002−0.04 and 0.02−0.15 au for ρ and $\nabla^2\rho$, respectively).

https://doi.org/10.1021/acsomega.1c04758
ACS Omega 2021, 6, 31971−31981

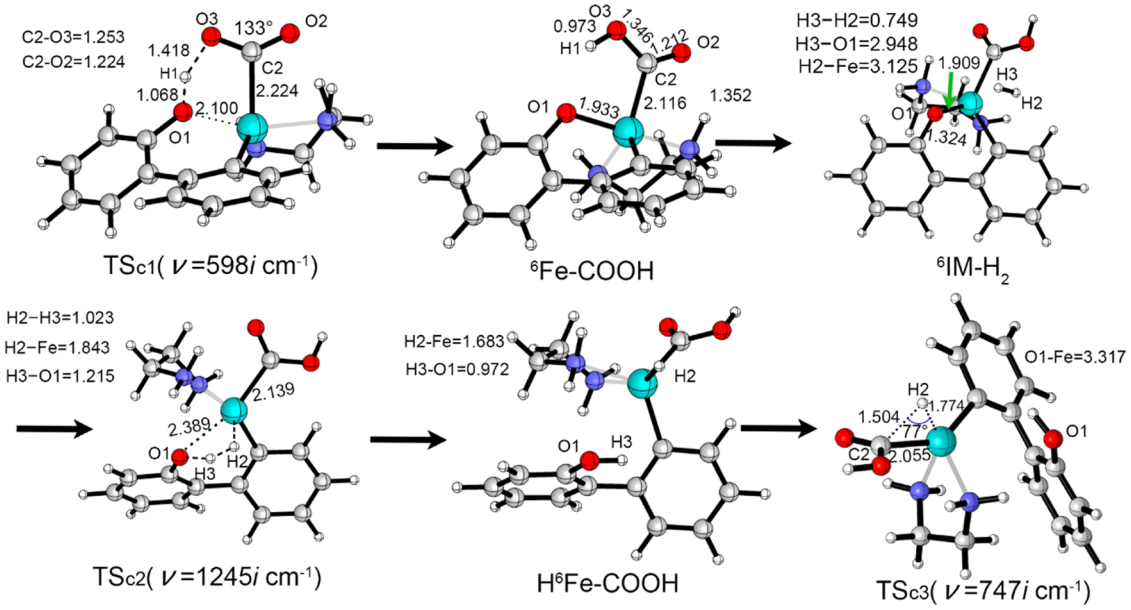

Figure 7. Evolution of optimized structures in the process of CO_2 reduction catalyzed by iron(I)-based complex at the doublet state **^{6}Fe(I)**. The bond distances are given in Å.

These data confirm the existence of hydrogen bonds O−H···O3 in **^{2}Fe-CO$_2$**. In **^{4}Fe-CO$_2$** and **^{6}Fe-CO$_2$**, the values of ρ and Laplacian $\nabla^2\rho$ are slightly larger than the top limit of the proposed criteria, leading to the speculation that the bonds O−H···O3 in **^{4}Fe-CO$_2$** and **^{6}Fe-CO$_2$** may be strong hydrogen bonds. Color-mapped RDG isosurface graphs and scatter diagrams of RDG versus sign $(\lambda^2)\rho$ for **^{2}Fe**, **^{4}Fe**, and **^{6}Fe** are shown in Figure S4 in the Supporting Information. In brief, there is a weak hydrogen bond in **^{2}Fe-CO$_2$** and a strong hydrogen bond in **^{4}Fe-CO$_2$** or **^{6}Fe-CO$_2$**. QTAIM analyses also confirmed the destruction of the original hydrogen bond O−H···C and the formation of the new O−H···O hydrogen bond in both **^{2}Fe-CO$_2$** and **^{4}Fe-CO$_2$**.

Reduction of CO_2 Catalyzed by Iron(I)-Based Complex at the ^{2}Fe(I), ^{4}Fe(I), and ^{6}Fe(I) Spin States. We continued the study of the reduction of CO_2 catalyzed by the iron(I)-based complex at its doublet, quartet, and sextet spin states, as the CO_2 reduction to formic acid and/or its derivatives has attracted enormous attention due to the potential applications. As presented above, while CO_2 is fixed on the Fe center, which could be in various **^{2}Fe(I)**, **^{4}Fe(I)**, or **^{6}Fe(I)** spin states, a hydrogen-bond exchange occurs. Consequently, it is very likely that a conceived cooperation promotes the formation of a −COOH moiety through a proton transfer from O1 to O3 of CO_2 and the formation of the O1−Fe bond through a hypothesized five-membered ring O1−H1−O3−C2−Fe. The generation of −COOH from CO_2 may be considered as an essential step in the CO_2 reduction to formic acid and its derivatives, and thus the iron(I)-based complex would provide an alternative access to the exploration of the CO_2 reduction.

As expected, we indeed located the transition state for the −COOH moiety formation through a proton transfer from O1 to the O3 of CO_2 (TSa1 for **^{2}Fe-CO$_2$**, TSb1 for **^{4}Fe-CO$_2$**, and TSc1 for **^{6}Fe-CO$_2$**), and the optimized structures are plotted in Figures 5, 6, and 7. In the three transition states, a five-membered O1−H1−O3−C2−Fe ring can be identified, and it results from a proton transfer from the O1 to O3 of CO_2 and the formation of the O1−Fe bond. The cooperativity leads to the formation of a −COOH moiety. In TSa1, the bond distances of O1−H1 and H1−O3 are 1.064 and 1.439 Å, respectively. In TSc1, those are 1.068 and 1.418 Å, respectively. However, in TSb1, the O1−H1 bond is stretched to 1.101 Å, and the H1−O3 bond is shortened to 1.352 Å. These differences indicate that the TSb1 state for **^{4}Fe-CO$_2$** is more favorable to the proton transfer from the O1 to O3 of CO_2 than the TSa1 state for **^{2}Fe-CO$_2$** and TSc1 state for **^{6}Fe-CO$_2$**. The consequence is that, in this step, the former has a barrier of only 0.5 kcal/mol, while the latter have barriers of 9.2 and 1.6 kcal/mol, respectively. The very low energy barrier of TSb1 is likely due to its precursor **^{4}Fe-CO$_2$** with strong hydrogen bonding. In contrast, for TSa1, its precursor **^{2}Fe-CO$_2$** only has a weak hydrogen bond. Our implication here is that hydrogen bonding may play a role in promoting proton transfers. In the present case, the proton transfer also shortens the distance of the Fe−O1 bond, which is 1.973 Å in TSa, 2.054 Å in TSb1, and 2.100 Å in TSc1. For comparison, the values are 2.213 Å in **^{2}Fe-CO$_2$**, 2.117 Å in **^{4}Fe-CO$_2$**, and 2.157 Å in **^{4}Fe-CO$_2$**.

After the proton transfer transition states, intermediates (**^{2}Fe-COOH**, **^{4}Fe-COOH**, and **^{6}Fe-COOH**) with a −COOH moiety can be obtained with the decreasing standard Gibbs free energy, and the optimized structures are depicted in Figures 5−7, respectively. A significant structural change is the formation of the O1−Fe bond in all intermediates.

To achieve the ultimate goal of generating formic acid, it is necessary for **^{2}Fe-COOH**, **^{4}Fe-COOH**, or **^{6}Fe-COOH** to carry out a hydrogenation (one H atom adding to the C2 atom in the −COOH moiety). Here, we proposed the use of H_2 gas as the H-atom source in the hydrogenation process. One H_2 molecule is first adsorbed by **^{2}Fe-COOH**, **^{4}Fe-COOH**, or **^{6}Fe-COOH** to form a slightly less stable intermediate ^{2}IM-H_2, ^{4}IM-H_2, or ^{6}IM-H_2, respectively, followed by the splitting of the H−H bond to form the iron hydride complex **H^{2}Fe-COOH**, **H^{4}Fe-COOH**, or **H^{6}Fe-COOH**. The H_2-adsorbed intermediates, the iron hydride complexes, and the H−H bond splitting transition states (TSa2, TSb2, and TSc2) are depicted in Figures 5−7, respectivey. The bond lengths of the adsorbed H_2

https://doi.org/10.1021/acsomega.1c04758
ACS Omega 2021, 6, 31971−31981

Scheme 1. Catalytic Cycle for CO_2 Reduction Catalyzed by the Iron(I)-Based Complex

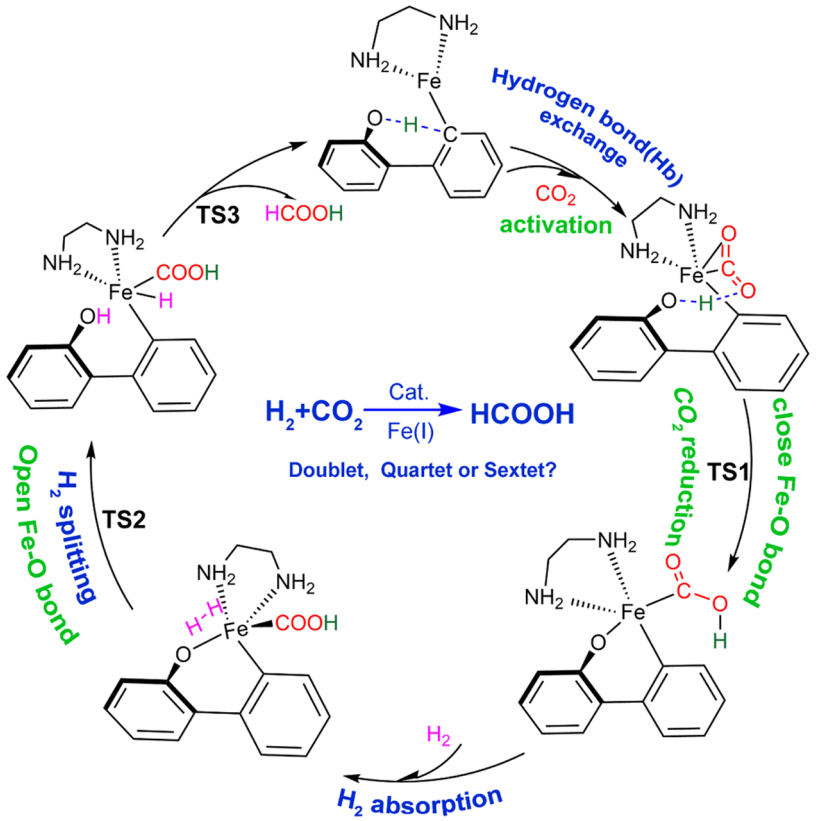

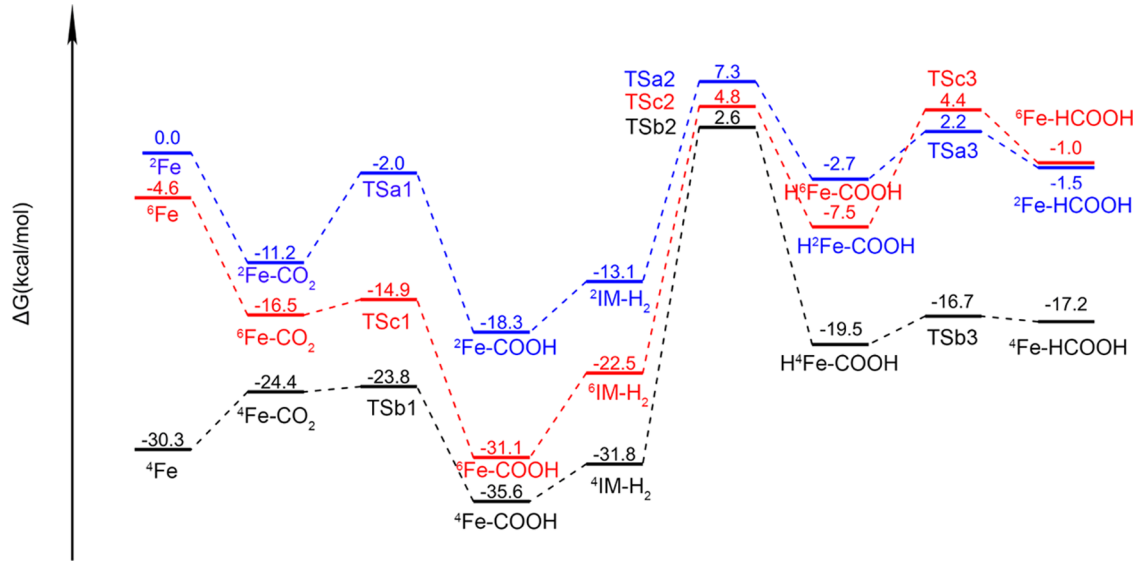

Figure 8. Free energy profiles for the CO_2 reduction catalyzed by the designed iron(I)-based complex at different states (doublet **^{2}Fe** in blue, quartet **^{4}Fe** in black, and sextet **^{6}Fe** in red).

are 0.811, 0.753, and 0.749 Å in ^{2}IM-H_2, ^{4}IM-H_2, and ^{6}IM-H_2, respectively, which are slightly longer than that of an isolated H_2, indicating that the adsorbed H_2 is activated in all states. However, the absorption of H_2 by **^{2}Fe-COOH**, **^{4}Fe-COOH**, and **^{6}Fe-COOH** are endergonic processes, requiring energy inputs of 5.2, 3.8, and 8.6 kcal/mol, respectively.

In the transition states leading to the H−H bond splitting, the hydrogen atoms are bound by both Fe and O1 atoms of the Fe−O1 bond, which is formed in the H1 proton transfer process, and the H−H distance is stretched to 1.046 in TSa2, 1.022 Å in TSb2, and 1.023 Å in TSc2. The O1−H3 distance is 1.251 Å, and the H2−Fe distance is 1.640 Å in TSa2; the O1−H3 distance is 1.212 Å, and the H2−Fe distance is 1.803 Å in TSb2; and the O1−H3 distance is 1.215 Å, and the H2−Fe distance is 1.843 Å in TSc2. Thus, H_2 splitting is a combined effort of both Fe and O1 atoms. However, the doublet state is more favorable for the H−H bond splitting than the quartet state and the quartet state, as in this step, their energy barriers are 20.4 versus 34.4 and 27.3 kcal/mol.

https://doi.org/10.1021/acsomega.1c04758
ACS Omega 2021, 6, 31971−31981

After undergoing the H−H bond splitting, the auxiliary group OH is recovered and the Fe−H2 bond is forged in the resulting iron hydride complex **H^{2}Fe-COOH**, **H^{4}Fe-COOH**, and **H^{6}Fe-COOH**, respectively. Early study has revealed that the iron hydride complexes exhibit strong reducibility and have been employed in the CO_2 reduction.[25] In **H^{2}Fe-COOH** and **H^{4}Fe-COOH**, the H2 of the Fe−H2 bond is close to neutral, and its NPA charges are only 0.05*e* and 0.04*e*, respectively. Differently, in **H^{6}Fe-COOH**, the NPA charge on the H2 atom is negative (−0.25*e*). However, the NPA charge indicates that the H2 of the Fe−H2 bond in all three states very likely exhibit strong reducibility. Therefore, the Fe−H2 bonds in **H^{2}Fe-COOH**, **H^{4}Fe-COOH**, and **H^{6}Fe-COOH** would provide a route to the formation of HCOOH through a hydrogen atom transfer from the Fe center to the C2 atom.

The route to the formation of HCOOH can be achieved through the H2-atom-transferred transition states (labeled as TSa3, TSb3, and TSc3 for the doublet, quartet, and sextet states, respectively), which are characterized with a three-membered ring mode, as depicted in Figures 5−7, respectively. In TSa3, the C2−H2 distance is 1.383 Å, while the H2−Fe distance is 1.599 Å, and their intersection angle is 79°; and in TSb3, the C2−H2 and H2−Fe bond distances are 1.743 and 1.565 Å, respectively, and their intersection angle is 74°. Similarly, in TSc3, the C2−H2 and H2−Fe bond distances are 1.504 and 1.774 Å, respectively, and their intersection angle is 77°. We also found that the three-membered ring mode is favorable for the H2 atom transfer, as the energy barriers are only 4.9, 2.8, and 11.9 kcal/mol for TSa3, TSb3, and TSc3, respectively. With the H2 atom transferred, the target product HCOOH attached to the iron(I)-based complex **^{2}Fe**, **^{4}Fe**, or **^{6}Fe** is generated.

Scheme 1 summarizes the complete route of the CO_2 reduction catalyzed by the designed iron(I)-based complex at all three spin states, and the energy flow charts for the reaction pathways are plotted in Figure 8. As shown in Figure 8, the absorption and splitting of H_2 via transition states TSa2, TSb2, and TSc2 is the rate-determining step in the whole process, with the total free energy barriers of 25.6, 37.2, and 35.9 kcal/mol, respectively. This suggests that the doublet structure of the iron(I)-based complex **^{2}Fe(I)** is considerably more favorable for the CO_2 reduction than the quartet state **^{4}Fe(I)** and the sextet state **^{6}Fe(I)**. The two earlier steps of the proton ($H1^+$) transfer and the H2 atom transfer proceed easily for all **^{2}Fe(I)**, **^{4}Fe(I)**, and **^{6}Fe(I)** states. It is further revealed that the hydrogen bond O−H···C1 and the five-membered O1−H1−O3−C2−Fe ring exert synergistic effect on the proton ($H1^+$) transfer and that the formation of the three-membered H2C2Fe ring facilitates the H2 atom transfer. It should be reminded that the CO_2 fixation by the **^{4}Fe** state to form the complex **^{4}Fe-CO$_2$** is an endergonic process with an increasing Gibbs free energy by 5.9 kcal/mol, even though **^{4}Fe(I)** is more thermodynamically stable than **^{2}Fe(I)** and **^{6}Fe(I)**. However, the strong absorptivity of **^{4}Fe(I)** could lead to a photosensitizer-free visible-light-mediated high−low spin shift to the less stable doublet state **^{2}Fe** through reverse intersystem crossing (RISC). In addition, from Scheme 1, an interesting finding is that the formation and break of the Fe−O bond are closely related to the two key steps in the CO_2 reduction process. That is to say, the formation of −COOH moiety from CO_2 is accompanied by Fe−O1 bond formation, and the splitting of one H_2 molecule is accompanied by Fe−O1 bond breaking. Therefore, the rationally designed iron(I)-based complexes **^{2}Fe** and **^{4}Fe** as well as **^{6}Fe** combining visible-light catalytic conditions all can be employed to catalyze the CO_2 reduction.

CONCLUSIONS

In this prospect work, we proposed an innovative strategy to explore the CO_2 reduction catalyzed by the theoretically designed low-valence iron(I) model complex at various spin states including the doublet state **^{2}Fe(I)**, the quartet state **^{4}Fe(I)**, and the sextet state **^{6}Fe(I)**, where the central iron(I) ion bonds to an ethanediamine (en) and a 2-hydroxy-biphenyl group. Computations revealed notable features in the process of the CO_2 reduction. First, CO_2 can be facilely fixed and activated by the univalent iron(I) complex. In sharp contrast, trivalent iron(III) and bivalent iron(II) compounds are able to capture and activate CO_2. Second, the low spin state **^{2}Fe(I)** is more favorable for the CO_2 reduction than the high spin state **^{4}Fe(I)** and **^{6}Fe(I)**, as the former has a much lower total free energy barrier than the latter. Still, the CO_2 reduction process can be initiated from the **^{4}Fe(I)** and **^{6}Fe(I)** states, as the photosensitizer-free visible-light-mediated high−low spin shift from **^{4}Fe(I)** and **^{6}Fe(I)** to **^{2}Fe(I)** can proceed through the reverse intersystem crossing (RISC). Third, there is a synergistic interaction between a hydrogen bonding and a five-membered ring, which promotes the proton transfer, leading to the formation of the −COOH moiety from CO_2. This is the key step for the CO_2 reduction to formic acid and/or its derivatives. Fourth, the H−H bond is essentially split by both Fe and O1 atoms of the Fe−O1 bond. The H_2 splitting not only recovers the auxiliary hydroxyl group but also serves as the hydrogen atom source. Fifth, the formation of the three-membered H2C2Fe ring facilitates the H2 atom transfer to form the target product HCOOH. Finally, the two key steps (the formation of −COOH moiety from CO_2 and the splitting of one H_2 molecule) in the CO_2 reduction process are closely related to the formation and break of the Fe−O bond in the studied system. The present study provides an alternative approach to the challenging CO_2 reduction, and we anticipate that this work can stimulate further theoretical and experimental studies on the catalytic applications of iron(I) complexes in the CO_2 reduction.

COMPUTATIONAL DETAILS

All DFT calculations in this work were performed using the Gaussian16 software package[44] with the Minnesota density functional (M06)[45−47] and the empirical dispersion correction D3 developed by Grimme et al.,[48,49] and the combination of the Def2TZVP basis set for Fe atom and the augmented correlation consistent basis set 6-311+G(d, p) for all nonmetal atoms.[50] In previous reports, Yang et al. performed a density functional theory calculation with the M06 functional to study Knçlker's iron cyclopentadienone complex.[29] Lefèvre et al. established that the Def2TZVP basis set for Fe atom combining with D3(BJ) classical dispersion correction leads to a correct qualitative prediction of the ground spin state of a benchmark of iron(I).[51] All geometries of reactants, transition states (TSs), and products were fully optimized without constraints and with the analytic gradients and Berny algorithms using the GEDIIS method. The convergence criteria for electronic structure calculations were set to the default values in Gaussian16. Vibrational frequency calculations at the same level were performed to confirm stationary

https://doi.org/10.1021/acsomega.1c04758
ACS Omega 2021, 6, 31971−31981

points as minima (zero imaginary frequency) or transition states (one imaginary frequency). In several cases, where the TSs could not be easily confirmed by the animation of their vibrations, intrinsic reaction coordinate (IRC)[52,53] calculations were performed to establish the connection of each TS to its corresponding reactant and product. In the derivation of Gibbs free energies, the temperature for the reactions is set at 298 K and the pressure is at 1 atm unless specified. The energy barriers of key transition states at different pressure are provided in Tables S1 in the Supporting Information (SI). The entropy change and the enthalpy change are evaluated and provided in Table S2. To examine the geometries derived with the M06 functional, we performed computations of the ^{2}**Fe(I)**, ^{4}**Fe(I)**, and ^{6}**Fe(I)** structures with other density functionals including B3LYP, PBE0, and Wb97XD, and found that the optimized geometric parameters with the M06 functional are consistent with those with other density functional (see Tables S3 in the Supporting Information (SI)). It should be mentioned that coupled cluster theory at the CCSD(T) level, multiconfigurational perturbation theory (CASPT2, NEVPT2), and multireference configuration interaction at the MRCISD+Q level are great benchmarking quantum chemistry methods for spin-state energetics of iron complexes,[51,54−58] which can check errors of the DFT approach. However, it may be too costly to perform the calculation of the present whole reaction route. Partial atomic charges and vertical ionization energies (IE) were calculated with the natural population analysis (NPA)[59−61] at the same M06-2X-D3/6-311+G(d,p)//Def2TZVP theoretical level. In addition, electrostatic potential (ESP)[41] and AIM analysis data were calculated using Multiwfn[41,42] and drawn with VMD.[62]

■ ASSOCIATED CONTENT

Supporting Information

The Supporting Information is available free of charge at https://pubs.acs.org/doi/10.1021/acsomega.1c04758.

> Key geometric parameters of ^{2}**Fe**, ^{4}**Fe**, and ^{6}**Fe** complexes at various density functions levels; comparison of the energy barriers of key transition states at different pressures; entropy change and enthalpy change for the CO_2 reduction catalyzed by the designed iron(I)-based complex at the different states; scatter graphs of **Fe(I)** and **Fe-CO$_2$** complexes with the doublet, quartet, and sextet spin states and the color graphs of the RDG isosurface; and optimized geometries of the designed Fe complex with trivalent iron(III) and bivalent iron(II) binding CO_2 and atomic coordinates of intermediates and key transition states (PDF)

■ AUTHOR INFORMATION

Corresponding Authors

Fang Ma − *School of Chemistry and Materials Science, Huaibei Normal University, Huaibei 235000, China;* orcid.org/0000-0001-7178-7232; Email: mafangchem@foxmail.com

Yirong Mo − *Department of Nanoscience, Joint School of Nanoscience and Nanoengineering, University of North Carolina at Greensboro, Greensboro, North Carolina 27401, United States;* orcid.org/0000-0002-2994-7754; Email: y_mo3@uncg.edu

Authors

Yazhou Li − *School of Chemistry and Materials Science, Huaibei Normal University, Huaibei 235000, China*

Xuhui Lin − *Sichuan Engineering Research Center for Biomimetic Synthesis of Natural Drugs, School of Life Science and Engineering, Southwest Jiaotong University, Chengdu 610031, China;* orcid.org/0000-0002-9654-5499

Complete contact information is available at: https://pubs.acs.org/10.1021/acsomega.1c04758

Notes

The authors declare no competing financial interest.

■ ACKNOWLEDGMENTS

This work was supported by the National Natural Science Foundation of China (no. 21303065), University Natural Science Foundation of Anhui Province (no. KJ2017A388), and Approving and Initiating the Cultivation Project of Excellent Top-notch Talent in Colleges and Universities in Anhui Province (no. gxfx2017037). This work was performed in part at the Joint School of Nanoscience and Nanoengineering, a member of the Southeastern Nanotechnology Infrastructure Corridor (SENIC), and National Nanotechnology Coordinated Infrastructure (NNCI), which is supported by the National Science Foundation (Grant ECCS-1542174).

■ REFERENCES

(1) Bhanage, B. M.; Arai, M. Transformation and Utilization of Carbon Dioxide. In *Green Chemistry and Sustainable Technology*; Springer: Berlin, Heidelberg, 2014.

(2) Plasseraud, L. *Carbon Dioxide As Chemical Feedstock*, Aresta, M., Eds.; John Wiley & Sons: 2010; Vol. 3, pp 631−632.

(3) Wang, W.; Wang, S.; Ma, X.; Gong, J. Recent Advances in Catalytic Hydrogenation of Carbon Dioxide. *Chem. Soc. Rev.* **2011**, *40*, 3703−3727.

(4) Gao, Y.; Cai, Z.; Li, S.; Li, G. Rhodium(I)-Catalyzed Aryl C−H Carboxylation of 2-Arylanilines with CO_2. *Org. Lett.* **2019**, *21*, 3663−3669.

(5) Cai, L.; Fu, L.; Zhou, C.; Gao, Y.; Li, S.; Li, G. Rh(i)-Catalyzed Regioselective Arylcarboxylation of Acrylamides with Arylboronic acids and CO_2. *Green Chem.* **2020**, *22*, 7328−7332.

(6) Metsänen, T. T.; Oestreich, M. Temperature-Dependent Chemoselective Hydrosilylation of Carbon Dioxide to Formaldehyde or Methanol Oxidation State. *Organometallics* **2015**, *34*, 543−546.

(7) Siebert, M.; Seibicke, M.; Siegle, A. F.; Kräh, S.; Trapp, O. Selective Ruthenium-Catalyzed Transformation of Carbon Dioxide: An Alternative Approach toward Formaldehyde. *J. Am. Chem. Soc.* **2019**, *141*, 334−341.

(8) Mathis, C. L.; Geary, J.; Ardon, Y.; Reese, M. S.; Philliber, M. A.; VanderLinden, R. T.; Saouma, C. T. Thermodynamic Analysis of Metal−ligand Cooperativity of PNP Ru Complexes: Implications for CO_2 Hydrogenation to Methanol and Catalyst Inhibition. *J. Am. Chem. Soc.* **2019**, *141*, 14317−14328.

(9) Schmeier, T. J.; Dobereiner, G. E.; Crabtree, R. H.; Hazari, N. Secondary Coordination Sphere Interactions Facilitate The Insertion Step in An Iridium(III) CO_2 Reduction Catalyst. *J. Am. Chem. Soc.* **2011**, *133*, 9274−9277.

(10) Takaoka, S.; Eizawa, A.; Kusumoto, S.; Nakajima, K.; Nishibayashi, Y.; Nozaki, K. Hydrogenation of Carbon Dioxide with Organic Base by PCIIP-Ir Catalysts. *Organometallics* **2018**, *37*, 3001−3009.

(11) Loipersberger, M.; Zee, D. Z.; Panetier, J. A.; Chang, C. J.; Long, J. R.; Head-Gordon, M. Computational Study of An Iron(II) Polypyridine Electrocatalyst for CO_2 Reduction: Key Roles for Intramolecular Interactions in CO_2 Binding and Proton Transfer. *Inorg. Chem.* **2020**, *59*, 8146−8160.

(12) Liu, R.; Ma, Z.; Sears, J. D.; Juneau, M.; Neidig, M. L.; Porosoff, M. D. Identifying Correlations in Fischer-Tropsch Synthesis and CO_2 Hydrogenation over Fe-Based ZSM-5 Catalysts. *J. CO2 Util.* **2020**, *41*, No. 101290.
(13) Jeletic, M. S.; Mock, M. T.; Appel, A. M.; Linehan, J. C. A Cobalt-based Catalyst for The Hydrogenation of CO_2 under Ambient Conditions. *J. Am. Chem. Soc.* **2013**, *135*, 11533−11536.
(14) Cramer, H. H.; Chatterjee, B.; Weyhermüller, T.; Werlé, C.; Leitner, W. Controlling The Product Platform of Carbon Dioxide Reduction: Adaptive Catalytic Hydrosilylation of CO_2 Using a Molecular Cobalt(II) Triazine Complex. *Angew. Chem., Int. Ed.* **2020**, *59*, 15674−15681.
(15) Moradi, G. R.; Rahmanzadeh, M.; Khosravian, F. The Effects of Partial Substitution of Ni by Zn in $LaNiO_3$ Perovskite Catalyst for Methane Dry Reforming. *J. CO2 Util.* **2014**, *6*, 7−11.
(16) Lücken, J.; Auth, T.; Mozzi, S. I.; Meyer, F. Hexanuclear Copper(I) Hydride from The Reduction-induced Decarboxylation of A Dicopper(II) Formate. *Inorg. Chem.* **2020**, *59*, 14347−14354.
(17) Shin, H.; Liu, X.; Lacelle, T.; MacDonell, R. J.; Schuurman, M. S.; Malenfant, P. R. L.; Paquet, C. Mechanistic Insight into Bis(amino) Copper Formate Thermochemistry for Conductive Molecular Ink Design. *ACS Appl. Mater. Interfaces* **2020**, *12*, 33039−33049.
(18) Reuillard, B.; Ly, K. H.; Rosser, T. E.; Kuehnel, M. F.; Zebger, I.; Reisner, E. Tuning Product Selectivity for Aqueous CO_2 Reduction with A Mn(bipyridine)-Pyrene Catalyst Immobilized on A Carbon Nanotube Electrode. *J. Am. Chem. Soc.* **2017**, *139*, 14425−14435.
(19) Wu, Z.-Z.; Gao, F.-Y.; Gao, M.-R. Regulating the oxidation state of nanomaterials for electrocatalytic CO_2 reduction. *Energy Environ. Sci.* **2021**, *14*, 1121−1139.
(20) Federsel, C.; Jackstell, R.; Beller, M. State-of-The-Art Catalysts for Hydrogenation of Carbon Dioxide. *Angew. Chem., Int. Ed.* **2010**, *49*, 6254−6257.
(21) Ziebart, C.; Federsel, C.; Anbarasan, P.; Jackstell, R.; Baumann, W.; Spannenberg, A.; Beller, M. Well-Defined Iron Catalyst for Improved Hydrogenation of Carbon Dioxide and Bicarbonate. *J. Am. Chem. Soc.* **2012**, *134*, 20701−20704.
(22) Rivada-Wheelaghan, O.; Dauth, A.; Leitus, G.; Diskin-Posner, Y.; Milstein, D. Synthesis and Reactivity of Iron Complexes with A New Pyrazine-Based Pincer Ligand, and Application in Catalytic Low-Pressure Hydrogenation of Carbon Dioxide. *Inorg. Chem.* **2015**, *54*, 4526−4538.
(23) Bertini, F.; Gorgas, N.; Stöger, B.; Peruzzini, M.; Veiros, L. F.; Kirchner, K.; Gonsalvi, L. Efficient and Mild Carbon Dioxide Hydrogenation to Formate Catalyzed by Fe(II) Hydrido Carbonyl Complexes Bearing 2,6-(Diaminopyridyl)diphosphine Pincer Ligands. *ACS Catal.* **2016**, *6*, 2889−2893.
(24) Bertini, F.; Mellone, I.; Ienco, A.; Peruzzini, M.; Gonsalvi, L. Iron(II) Complexes of The Linear Rac-Tetraphos-1 Ligand as Efficient Homogeneous Catalysts for Sodium Bicarbonate Hydrogenation and Formic Acid Dehydrogenation. *ACS Catal.* **2015**, *5*, 1254−1265.
(25) Jayarathne, U.; Hazari, N.; Bernskoetter, W. H. Selective Iron-Catalyzed N-Formylation of Amines Using Dihydrogen and Carbon Dioxide. *ACS Catal.* **2018**, *8*, 1338−1345.
(26) Zhang, Y.; MacIntosh, A. D.; Wong, J. L.; Bielinski, E. A.; Williard, P. G.; Mercado, B. Q.; Hazari, N.; Bernskoetter, W. H. Iron Catalyzed CO_2 Hydrogenation to Formate Enhanced by Lewis Acid Co-Catalysts. *Chem. Sci.* **2015**, *6*, 4291−4299.
(27) Zhu, F.; Zhu-Ge, L.; Yang, G.; Zhou, S. Iron-Catalyzed Hydrogenation of Bicarbonates and Carbon Dioxide to Formates. *ChemSusChem* **2015**, *8*, 609−612.
(28) Coufourier, S.; Gaignard Gaillard, Q.; Lohier, J.-F.; Poater, A.; Gaillard, S.; Renaud, J.-L. Hydrogenation of CO_2, Hydrogenocarbonate, and Carbonate to Formate in Water Using Phosphine Free Bifunctional Iron Complexes. *ACS Catal.* **2020**, *10*, 2108−2116.
(29) Ge, H.; Chen, X.; Yang, X. Hydrogenation of Carbon Dioxide to Methanol Catalyzed by Iron, Cobalt, and Manganese Cyclopentadienone Complexes: Mechanistic Insights and Computational Design. *Chem. - Eur. J.* **2017**, *23*, 8850−8856.
(30) Wilding, M. J. T.; Iovan, D. A.; Betley, T. A. High-Spin Iron Imido Complexes Competent for C−H Bond Amination. *J. Am. Chem. Soc.* **2017**, *139*, 12043−12049.
(31) Kleinhaus, J. T.; Wittkamp, F.; Yadav, S.; Siegmund, D.; Apfel, U.-P. [FeFe]-Hydrogenases: Maturation and Reactivity of eEnzymatic Systems and Overview of Biomimetic Models. *Chem. Soc. Rev.* **2021**, *50*, 1668−1784.
(32) Bonetto, R.; Altieri, R.; Tagliapietra, M.; Barbon, A.; Bonchio, M.; Robert, M.; Sartorel, A. Electrochemical Conversion of CO_2 to CO by a Competent Fe(I) Intermediate Bearing a Schiff Base Ligand. *ChemSusChem* **2020**, *13*, 4111−4120.
(33) Ott, J. C.; Wadepohl, H.; Gade, L. H. Opening Up The Valence Shell: A T-shaped Iron(I) Metalloradical and Its Potential for Atom Abstraction. *Angew. Chem., Int. Ed.* **2020**, *59*, 9448−9452.
(34) Ouyang, Z.; Cheng, J.; Li, L.; Bao, X.; Deng, L. High-Spin Iron(I) and Iron(0) Dinitrogen Complexes Supported by N-Heterocyclic Carbene Ligands. *Chem. - Eur. J.* **2016**, *22*, 14162−14165.
(35) Lipschutz, M. I.; Chantarojsiri, T.; Dong, Y.; Tilley, T. D. Synthesis, Characterization, and Alkyne Trimerization Catalysis of A Heteroleptic Two-Coordinate Fe(I) Complex. *J. Am. Chem. Soc.* **2015**, *137*, 6366−6372.
(36) Hou, Q.; Wu, Y.; Zhou, S.; Wei, Y.; Caro, J.; Wang, H. Ultra-Tuning of The Aperture Size in Stiffened ZIF-8_Cm Frameworks with Mixed-Linker Strategy for Enhanced CO_2/CH_4 Separation. *Angew. Chem., Int. Ed.* **2019**, *58*, 2.
(37) Bauer, I.; Knölker, H.-J. Iron Catalysis in Organic Synthesis. *Chem. Rev.* **2015**, *115*, 3170−3387.
(38) Bauer, G.; Hu, X. Recent Developments of Iron Pincer Complexes for Catalytic Applications. *Inorg. Chem. Front.* **2016**, *3*, 741−765.
(39) Hu, D.; Yao, L.; Yang, B.; Ma, Y. Reverse Intersystem Crossing from Upper Triplet Levels to Excited Singlet: A 'Hot Excition' Path for Organic Light-Emitting Diodes". *Philos. Trans. R. Soc., A* **2015**, *373*, No. 20140318.
(40) Rohatgi-Mukherjee, K. K. *Fundamentals of Photochemistry*; Wiley Eastern: New Delhi, India, 1978.
(41) Lu, T.; Manzetti, S. Wavefunction and Reactivity Study of Benzo[a]pyrene Diol Epoxide and Its Enantiomeric Forms. *Struct. Chem.* **2014**, *25*, 1521−1533.
(42) Lu, T.; Chen, F. Multiwfn: A Multifunctional Wavefunction Analyzer. *J. Comput. Chem.* **2012**, *33*, 580−592.
(43) Lipkowski, L.; Grabowski, S. J.; Robinson, T. L.; Leszczynski, J. Properties of The C−H···H Dihydrogen Bond: An Bb Initio and Topological Analysis. *J. Phys.Chem. A* **2004**, *108*, 10865−10872.
(44) Frisch, M. J.; Trucks, G. W.; Schlegel, H. B.; Scuseria, G. E.; Robb, M. A.; Cheeseman, J. R.; Scalmani, G.; Barone, V.; Petersson, G. A.; Nakatsuji, H.; Li, X.; Caricato, M.; Marenich, A. V.; Bloino, J.; Janesko, B. G.; Gomperts, R.; Mennucci, B.; Hratchian, H. P.; Ortiz, J. V.; Izmaylov, A. F.; Sonnenberg, J. L.; Williams; Ding, F.; Lipparini, F.; Egidi, F.; Goings, J.; Peng, B.; Petrone, A.; Henderson, T.; Ranasinghe, D.; Zakrzewski, V. G.; Gao, J.; Rega, N.; Zheng, G.; Liang, W.; Hada, M.; Ehara, M.; Toyota, K.; Fukuda, R.; Hasegawa, J.; Ishida, M.; Nakajima, T.; Honda, Y.; Kitao, O.; Nakai, H.; Vreven, T.; Throssell, K.; Montgomery, J. A., Jr.; Peralta, J. E.; Ogliaro, F.; Bearpark, M. J.; Heyd, J. J.; Brothers, E. N.; Kudin, K. N.; Staroverov, V. N.; Keith, T. A.; Kobayashi, R.; Normand, J.; Raghavachari, K.; Rendell, A. P.; Burant, J. C.; Iyengar, S. S.; Tomasi, J.; Cossi, M.; Millam, J. M.; Klene, M.; Adamo, C.; Cammi, R.; Ochterski, J. W.; Martin, R. L.; Morokuma, K.; Farkas, O.; Foresman, J. B.; Fox, D. J.. *Gaussian 16*, Rev. B.01, Wallingford, CT, 2016.
(45) Zhao, Y.; Truhlar, D. G. A New Local Density Functional for Main-Group Thermochemistry, Transition Metal Bonding, Thermochemical Kinetics, and Noncovalent Interactions. *J. Chem. Phys.* **2006**, *125*, No. 194101.
(46) Zhao, Y.; Truhlar, D. G. The M06 Suite of Density Functionals for Main Group Thermochemistry, Thermochemical Kinetics,

https://doi.org/10.1021/acsomega.1c04758
ACS Omega 2021, 6, 31971−31981

Noncovalent Interactions, Excited States, and Transition Elements: Two New Functionals and Systematic Testing of Four M06-Class Functionals and 12 Other Functionals. *Theor. Chem. Acc.* **2008**, *120*, 215−241.
(47) Zhao, Y.; Schultz, N. E.; Truhlar, D. G. Exchange-Correlation Functional with Broad Accuracy for Metallic and Nonmetallic Compounds, Kinetics, and Noncovalent Interactions. *J. Chem. Phys.* **2005**, *123*, No. 161103.
(48) Grimme, S.; Antony, J.; Ehrlich, S.; Krieg, H. A Consistent and Accurate Ab Initio Parametrization of Density Functional Dispersion Correction (DFT-D) for The 94 Elements H-Pu. *J. Chem. Phys.* **2010**, *132*, No. 154104.
(49) Singla, P.; Riyaz, M.; Singhal, S.; Goel, N. Theoretical Study of Adsorption of Amino Acids on Graphene and BN Sheet in Gas and Aqueous Phase with Empirical DFT Dispersion Correction. *Phys. Chem. Chem. Phys.* **2016**, *18*, 5597−5604.
(50) Hehre, W. J.; Ditchfield, R.; Pople, J. A. Self—Consistent Molecular Orbital Methods. XII. Further Extensions of Gaussian—Type Basis Sets for Use in Molecular Orbital Studies of Organic Molecules. *J. Chem. Phys.* **1972**, *56*, 2257−2261.
(51) Rousseau, L.; Brémond, E.; Lefèvre, G. Assessment of The Ground Spin State of Iron(I) Complexes: Insights from DFT Predictive Models. *New J. Chem.* **2018**, *42*, 7612−7616.
(52) Fukui, K. The Path of Chemical Reactions - The IRC Approach. *Acc. Chem. Res.* **1981**, *14*, 363−368.
(53) Fukui, K. Formulation of The Reaction Coordinate. *J. Phys. Chem. A.* **1970**, *74*, 4161−4163.
(54) Radoń, M.; Gąssowska, K.; Szklarzewicz, J.; Broclawik, E. Spin-State Energetics of Fe(III) and Ru(III) Aqua Complexes: Accurate ab Initio Calculations and Evidence for Huge Solvation Effects. *J. Chem. Theory Comput.* **2016**, *12*, 1592−1605.
(55) Cirera, J.; Via-Nadal, M.; Ruiz, E. Benchmarking Density Functional Methods for Calculation of State Energies of First Row Spin-Crossover Molecules. *Inorg. Chem.* **2018**, *57*, 14097−14105.
(56) Radoń, M. Benchmarking Quantum Chemistry Methods for Spin-State Energetics of Iron Complexes against Quantitative Experimental Data. *Phys. Chem. Chem. Phys.* **2019**, *21*, 4854.
(57) Pierloot, K.; Phung, Q.; Domingo, A. Spin State Energetics in First-Row Transition Metal Complexes: Contribution of (3s3p) Correlation and Its Description by Second- Order Perturbation Theory. *J. Chem. Theory Comput.* **2017**, *13*, 537−553.
(58) Phung, Q.; Wouters, S.; Pierloot, K. Cumulant Approximated Second-Order Perturbation Theory Based on the Density Matrix Renormalization Group for Transition Metal Complexes: A Benchmark Study. *J. Chem. Theory Comput.* **2016**, *12*, 4352−4361.
(59) Reed, A. E.; Weinstock, R. B.; Weinhold, F. Natural Population Analysis. *J. Chem. Phys.* **1985**, *83*, 735−746.
(60) Carpenter, J. E.; Weinhold, F. Analysis of the Geometry of the Hydroxymethyl Radical by the "Different Hybrids for Different Spins" Natural Bond Orbital Procedure. *J. Mol. Struct.: THEOCHEM* **1988**, *169*, 41−62.
(61) Glendenig, E. D.; Badenhoop, J. K.; Reed, A. E.; Carpenter, J. E.; Bohmann, J. A.; Morales, C. M.; Weinhold, F. *NBO 5.0*; Theoretical Chemistry Institute University of Wisconsin: Madison, 2001.
(62) Humphrey, W.; Dalke, A.; Schulten, K. VMD: Visual Molecular Dynamics. *J. Mol. Graphics* **1996**, *14*, 33−38.

https://doi.org/10.1021/acsomega.1c04758
ACS Omega 2021, 6, 31971−31981